Transactions, **SMiRT-26**
Berlin/Potsdam, Germany, July 10-15, 2022
Division V

LARGE-SCALE SHEAR CRITICAL REINFORCED CONCRETE DEEP BEAM EXPERIMENTS MONITORED WITH FULL FIELD OF VIEW DIGITAL IMAGE CORRELATION EQUIPMENT

Dhanushka K. Palipana[1], Giorgio T. Proestos[2]

[1] Doctoral Candidate, Department of Civil, Construction and Environmental Engineering, North Carolina State University, Raleigh, NC, USA
[2] Assistant Professor, Department of Civil, Construction and Environmental Engineering, North Carolina State University, Raleigh, NC, USA (gproestos@ncsu.edu)

ABSTRACT

Reinforced concrete deep beams are common structural elements in nuclear facilities that are used to transfer large loads. They are shear critical and do not adhere to traditional beam bending theory. As various technologies in the nuclear industry continue to develop, such as AI-enhanced digital twin technology for use in structural assessments, detailed measurement data of structural performance is needed throughout loading to help inform these new technologies. This paper presents the results from an experimental series, the CCR series, of six large-scale reinforced concrete deep beam experiments monitored with full field of view, three-dimensional Digital Image Correlation (DIC) equipment. Varying shear span-to-depth ratios and loading plate sizes were considered in order to examine different critical crack angles. Both symmetrical and asymmetrical loading configurations were applied to simulate the response of members subjected to complex loading conditions. The paper summarizes the load-displacement data and strain field data of the deep beams tested and discusses the differences in performance for the variables investigated. The paper also compares the measured response of the deep beams with the predicted response from the nonlinear finite element program VecTor2 and the Two-Parameter Kinematic Theory (2PKT), a kinematic model for deep beams. The crack patterns of the beams obtained from DIC data are compared with observed crack patterns and crack patterns predicted by VecTor2. The results suggest that DIC can be used to guide the assessment of concrete nuclear facility components and that the response of such members is reasonably predicted by VecTor2 and the 2PKT.

INTRODUCTION

Reinforced concrete deep beams are common structural elements in nuclear facilities that are used to transfer large loads (see Figure 1). Reinforced concrete deep beams, which have shear span-to-depth ratios less than 2 or 2.5, are often shear critical and can fail in a brittle manner. These structural elements do not adhere to traditional beam bending theory, plane-sections-do-not-remain-plane and shear deformations dominate the response. Understanding deep beam response is therefore important to successfully design, assess and maintain nuclear facilities. Additionally, as the nuclear industry moves towards more affordable construction and maintenance practices, the use of AI-enhanced digital twin technologies may be able to reduce costs and better quantify risks throughout the life of structures. See, for example, Spencer et al. (2019). However, to train these data driven techniques and predict maintenance requirements, detailed measurement data of structural performance is needed throughout loading. The characterization of structural performance includes quantifying the load-deformation response, the deformation field of the entire structural element, and mapping the location, orientation and magnitude of crack widths and crack slips.

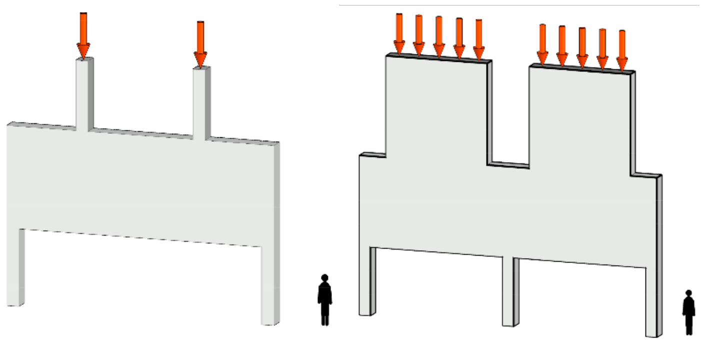

Figure 1. Transfer girders supporting columns and walls.

Digital Image Correlation (DIC) is a non-contact, optical data acquisition technology that can track 2D and 3D deformations on the surface of an object. A speckle pattern is applied on the surface of the object and cameras record the characteristics of the surface, in image pixels. DIC analysis software tracks the subsets of pixels based on the unique grey value information using an image correlation algorithm to obtain the movement of the surface. The displacement fields can then be used to compute strain fields, global kinematics or crack kinematics. See Sutton et al. (2009) and Mata-Falcón et al. (2020).

In this paper, a series of six large scale reinforced concrete deep beam experiments monitored with full field of view DIC is presented. In addition to varying shear span-to-depth ratios and loading plate sizes, both symmetrical and asymmetrical loading cases were examined to represent more complex loading configurations that occur in structures. The load-displacement responses, principal strain fields and the crack patterns obtained using DIC are then presented. The specimens were also modelled using the nonlinear finite element program, VecTor2 and the predicted load-displacement response, stress fields, crack patterns and the ultimate load are compared with the experimental results. The paper also compares the predicted deformation shape and the ultimate load predicted by the Two-Parameter Kinematic Theory (2PKT), a kinematic model for deep beams proposed by Mihaylov et al. (2013).

EXPERIMENTAL PROGRAM

An experimental series, the CCR series, of six large-scale reinforced concrete deep beam experiments monitored with full field of view, three-dimensional DIC equipment was conducted at the Constructed Facilities Laboratory at North Carolina State University. The beams were simply supported and measured 4877 x 1105 x 305 mm. The effective depth of the specimens was 909 mm. The specimens contained 9 #9 bars as bottom longitudinal reinforcement and 2 #9 bars as top longitudinal reinforcement. The transverse reinforcement, #3 stirrups, were spaced at 330 mm, giving a transverse reinforcement ratio of 0.141%. The geometric and reinforcement details are shown in Figure 2. The shear span-to-depth ratios and the loading plate size were varied in each test, as given in Table 1. CCR1-CCR3 were symmetrically loaded and had equal loading plate sizes (see Figure 2a), while CCR4-CCR6 were asymmetrically loaded. For CCR4 and CCR6, the loading was applied 203 mm and 127 mm offset from the centre of the symmetrically arranged loading plate, respectively (see Figure 2b). In CCR5, the loading plate was offset 318 mm from the centre of the beam and a centred load was applied on the loading plate (see Figure 2c). Therefore, each side of CCR4-CCR6 had different shear span lengths. These asymmetrical loading cases represent more complex geometrical configurations such as flexural moments in supported members being applied to the top of the deep beam, as may arise in seismic conditions. See Proestos et al. (2018), Qambar (2020) and Proestos et al. (2021).

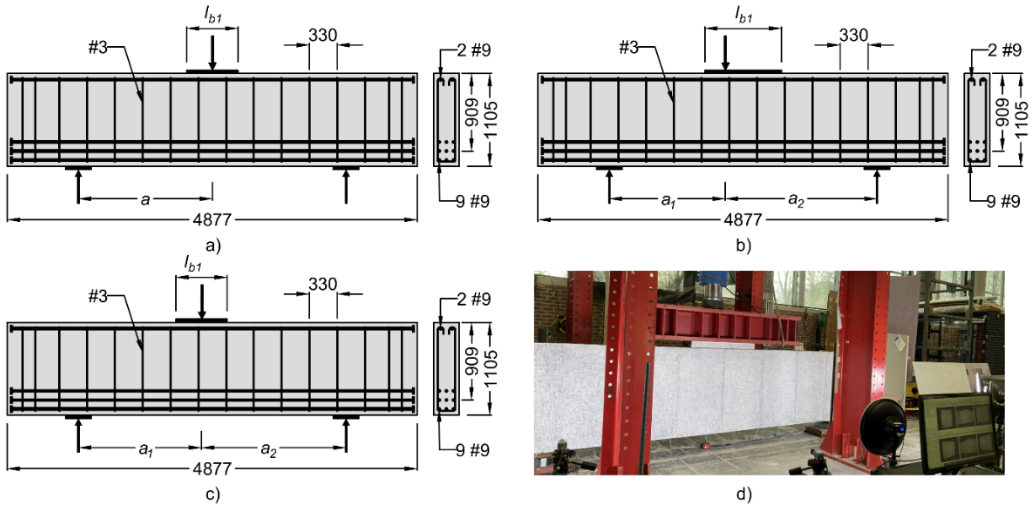

Figure 2. a) Geometric and reinforcement details of CCR1-CCR3, b) Geometric and reinforcement details of CCR4 and CCR6, c) Geometric and reinforcement details of CCR5, d) Collecting deformation data using DIC on the west face of the specimen.

Three-dimensional DIC was used to capture the full deformation field on the west face of the specimens, throughout loading. To maintain sufficient resolution in the data, three stereo systems were used. A built-in multi-view registration algorithm in the DIC analysis software was used to combine the displacement and strain field data obtained using the three systems.

The actuator load was increased monotonically to failure. Initially, flexural cracks appeared near midspan and propagated from the bottom of the beam. With an increase of the load, flexural cracks widened and shear cracks formed between the support plate and near the edge of the loading plate. As the loading continued, shear cracks extended, widened and ultimately all the specimens failed in shear. A summary of the experimental results including the peak applied load attained by each specimen is given in Table 1. No splitting cracks were observed along longitudinal reinforcement at any point during the test. Throughout the tests load stages were conducted. At a load stage the loading was halted and reduced by approximately 10% at which point the cracks were marked and measured on the east face of the specimen. During these load stages, high resolution photos were taken to record the crack patterns at that stage. CCR3 was reloaded after the peak load was reached to determine the residual capacity, however the maximum peak load had been already been attained.

Table 1: Summary of test specimen properties and peak applied loads.

Specimen	f_c' (MPa)	a/d (North)	a/d (South)	Failure span	l_{b1} (mm)	Peak applied load (kN)
CCR1	34.5	2.25	2.25	South	610	1916
CCR2	35.8	2.00	2.00	North	610	2235
CCR3	39.5	1.80	1.80	South	610	2614
CCR4	37.8	1.80	2.25	North	914	2333
CCR5	41.5	1.80	2.50	South	610	1765
CCR6	39.3	2.11	2.39	North	914	1816

EXPERIMENTAL RESULTS AND DISCUSSION

This section presents the experimental load versus displacement data, principal strains obtained using DIC, displacement fields and crack patterns for the six specimens examined. These results are then compared with the predicted response from the nonlinear finite element program VecTor2 and the Two-Parameter Kinematic Theory (2PKT).

Figure 3 shows the load versus the displacement at the bottom of the beam under the loading point obtained using DIC data. Comparing CCR1-CCR3, which had similar loading plate sizes, indicates that the ultimate strength of the specimens increases with decreasing *a/d* ratio, and the displacement at the peak load of the specimens decreases with decreasing *a/d* ratio. CCR5 and CCR6 which had different *a/d* and l_{b1} values had a similar load-displacement response. This is likely be due to the combined effect of varying *a/d* and l_{b1} of the two spans in each specimen. Additionally, the response of the specimens depends on the specific critical crack geometry, which significantly influences the contribution of different shear transfer mechanisms. See Palipana et al. (2021), Trandafir et al. (2022) and Palipana et al. (2022).

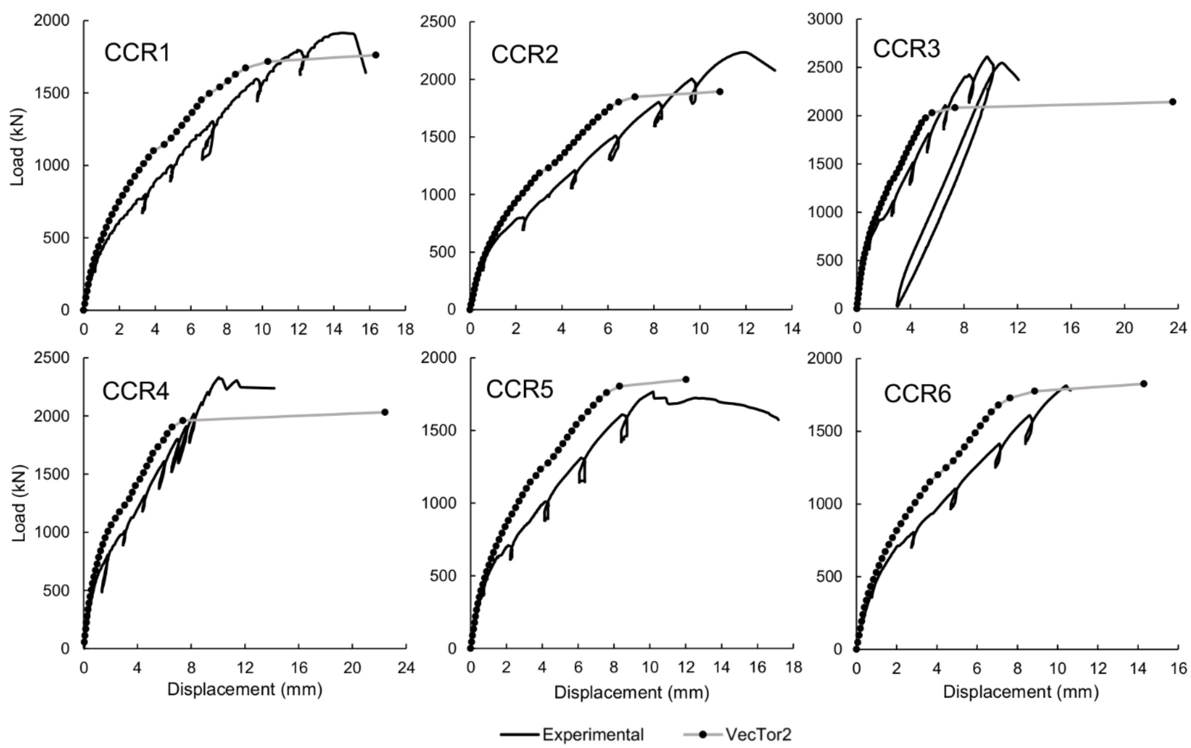

Figure 3. Load versus displacement at the bottom of the beam under the loading plate for CCR1-CCR6.

Figure 4 shows the principal tensile and compressive strain fields obtained at the peak load for CCR1-CCR6. Locally, the data at locations of spalling and areas where very large cracks occur are typically lost as a result of a loss of correlation in the speckle pattern. The high strain regions in the principle tensile strain plots (left) also help indicate areas of significant cracking. As can be seen in the data, at the peak load, the critical cracks in the members, defined as the crack that extends from the inner edge of support plate to near the edge of the loading plate and has largest crack width, have fully propagated for all the specimens. The region above the critical crack shows relatively small strains, which indicates that this region mostly behaves as a rigid body. The region between the critical cracks, in the so-called fanning region, is highly cracked. These observations are consistent with the observations of Mihaylov et al. (2013).

Figure 4 also shows the principal compressive strain plots for CCR1-CCR6 at the peak load (right). These strain maps help show the load arching from the loading plate to the support plate along compression struts that form in the member. These plots also show high compressive strain concentrations under the loading plate. In CCR1-CCR3, where loading was applied symmetrically, the edges of the loading plates show the largest strain concentrations. This is consistent with observations form Qambar (2020) and Proestos et al. (2021) who commented on the strain distributions under wide loading elements. For asymmetric loading conditions, the strain concentrations occur on the short shear span side of the loading plate, see CCR4-CCR6. In these cases, the specimens ultimately failed on the span with highly compressed edge of the loading plate.

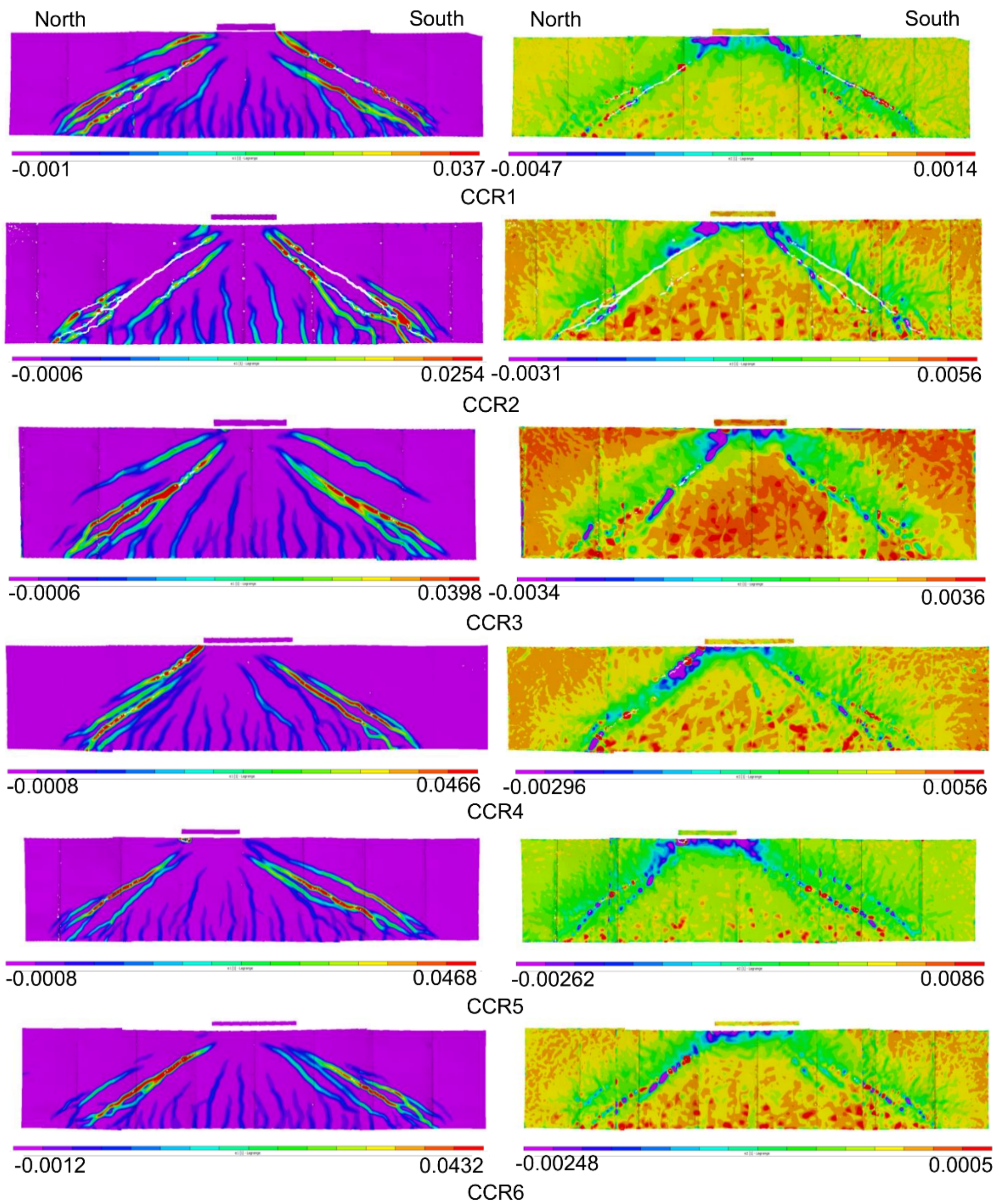

Figure 4. Principal tensile (left) and compressive (right) strain fields at the peak load of CCR1-CCR6.

As mentioned above, previous studies have shown that in addition to a/d and l_{b1}, specific crack geometry influences the strength of deep beams. See Palipana et al. (2021), Trandafir et al. (2022) and Palipana et al. (2022). Therefore, the crack patterns of the six specimens were examined in detail. The crack patterns on the east face of the specimens shortly after failure are shown in Figure 5 (left). CCR1-CCR3 shows that the angle of the cracks steepens as the a/d ratio decreases. When the beams are asymmetrically loaded, the cracks on the longer shear span terminate some distance inside and under the loading plate resulting in shallower cracks, whereas on the short shear span the critical crack tends to propagate to the edge of the loading plate resulting steeper cracks. (See CCR4 and CCR6 in Figure 5).

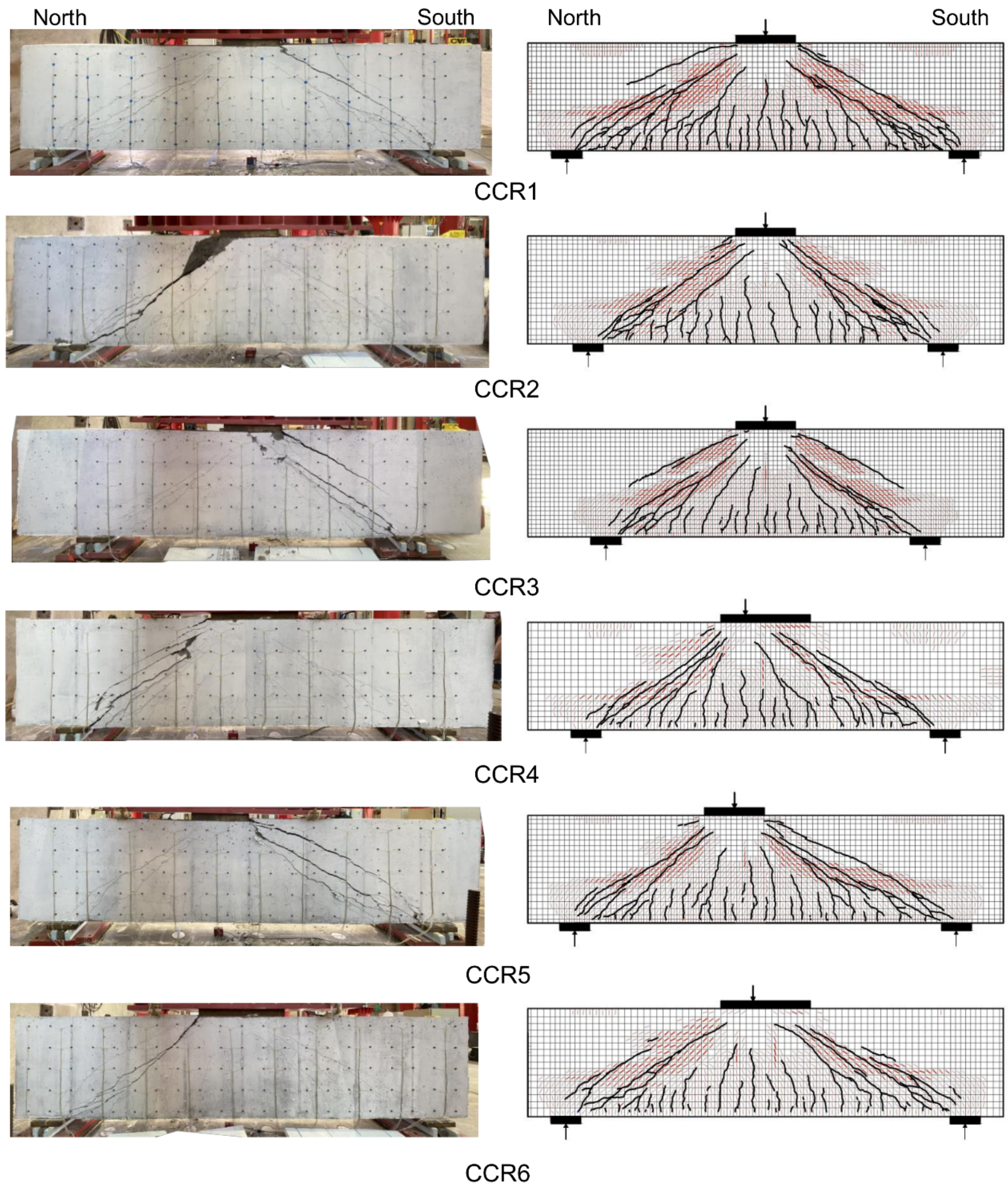

Figure 5. Comparison of crack patterns on the east face of specimens at failure (left), crack patterns obtained using DIC (right) and crack patterns predicted using VecTor2 (right) at the peak load of CCR1-CCR6.

Figure 5 also depicts the crack patterns obtained using DIC data, see black lines on the right. A new method called the Automated Crack Detection and Measurement (ACDM) tool was used to obtain crack patterns of the specimens using DIC data. The ACDM is an open-source MATLAB tool, developed by Gheri et al. (2020) that detects the cracks using high principal strain regions (see Figure 6a and 6b). When the principal strain fields obtained using DIC are input to the ACDM tool, it identifies the high tensile strain regions using two-dimensional image processing methods and the threshold defined by the user. The detected high strain regions in this way are thinned to obtain crack lines. The crack patterns obtained for the three stereo systems of each specimen were combined to generate the full crack patterns at the peak load on the west face of the specimens. Figure 5 (right) depicts the crack patterns obtained using the ACDM approach in conjunction with the DIC data. The crack patterns agree well with the crack patterns on the east face of the specimens, see Figure 5 (left).

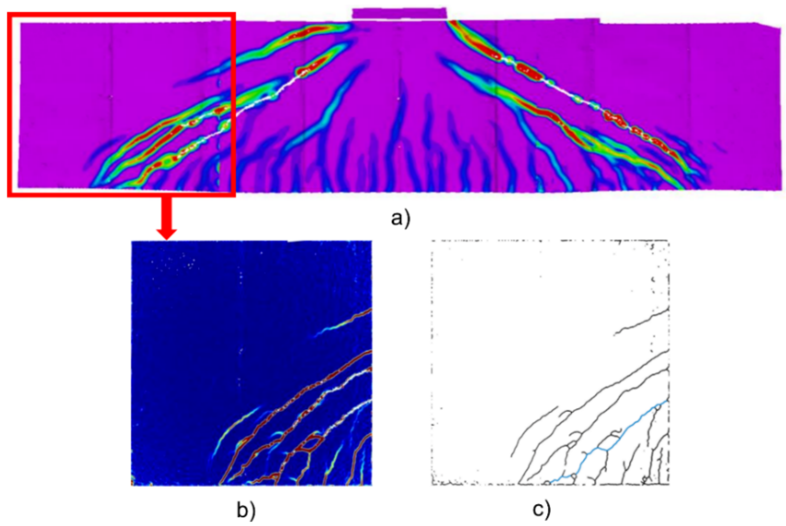

Figure 6. Crack information using ACDM for CCR1 north system a) DIC data obtained using three stereo systems for CCR1, b) Input principal strain fields obtained using DIC to ACDM tool and c) Cracks detected by ACDM tool from high tensile strain regions.

The experimental results were then compared with the response predicted using the VecTor2 finite element program. The beams were modelled using rectangular elements for concrete and truss elements for the longitudinal reinforcement. Transverse reinforcement was modelled as smeared reinforcement. To model the concrete behaviour Modified Popovics stress-strain relationship described by Collins and Mitchel was used. See Popovics (1970) and Collins and Mitchell (1991). A model defined using the experimentally obtained yield point, plastic plateau and strain hardening was used for the steel stress-strain relationship. The Young's modulus (E), yield strength (f_y), strain hardening strain (ε_{sh}), ultimate strength (f_u) and ultimate strain (ε_u) were taken as 200 GPa, 610 MPa, 10.4×10^{-3}, 783 MPa and 110.4×10^{-3} respectively for longitudinal reinforcement and 200 GPa, 494 MPa, 9×10^{-3}, 757 MPa and 136.1×10^{-3} respectively for transverse reinforcement. Figure 7 shows the principal compressive stresses-to-maximum softened compressive strength ratio (f_2/f_{2max}) predicted using these VecTor2 models at peak load. The plots show the compressive struts and stress concentrations near the loading plate corroborating what is observed in the DIC data (see Figure 4). The predicted load-displacement response for all six beams using VecTor2 is shown in Figure 3. The predicted and the experimentally observed uncracked stiffnesses agree well. However, VecTor2 predicts a somewhat stiffer cracked response for the members. For all specimens the predicted peak load is somewhat lower than the experimental peak load, except for CCR5. All the models correctly predict shear failures of the specimens. It should be noted that the large predicted displacements at the failure of the specimens is due to the very high loads and strains at the last converged load stage. The crack patterns predicted using the VecTor2 program are compared with the crack patterns generated using the ACDM tool in Figure 5 (right). The predicted angle of the cracks for each crack segment is shown by the red line segments in each element of the finite element mesh. The predicted crack angles agree well with the experimentally observed cracks.

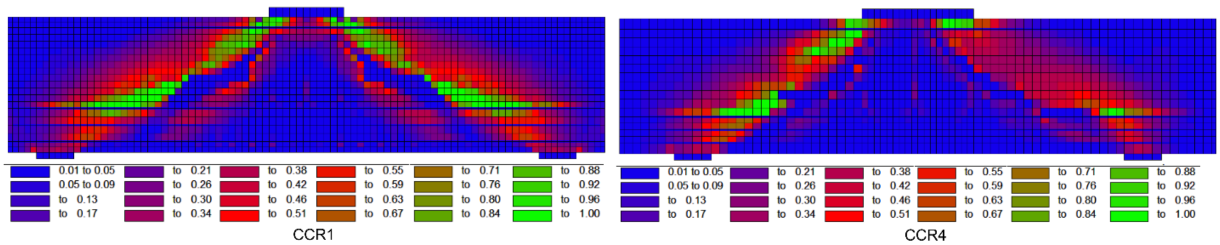

Figure 7. Predicted principal compressive stresses-to-maximum softened compressive strength ratio (f_2/f_{2max}) at failure from VecTor2 for CCR1 and CCR4.

Figure 8 shows the deformed shape of CCR1 and CCR2 obtained using DIC data at the peak load. The deformations are ×20 magnified. The deformation pattern is compared with the deformation shape predicted using the 2PKT, with ×20 magnification. The comparison shows that the displaced shapes in the fanning regions are very well predicted. The overall vertical displacement of the rigid body region above the critical crack are predicted satisfactorily by the 2PKT. However, there are some additional elastic deformations above the crack that are ignored in the 2PKT but are measured by DIC. The region near the crack at the bottom fibre are sensitive to the crack shape and thus the results are reasonable.

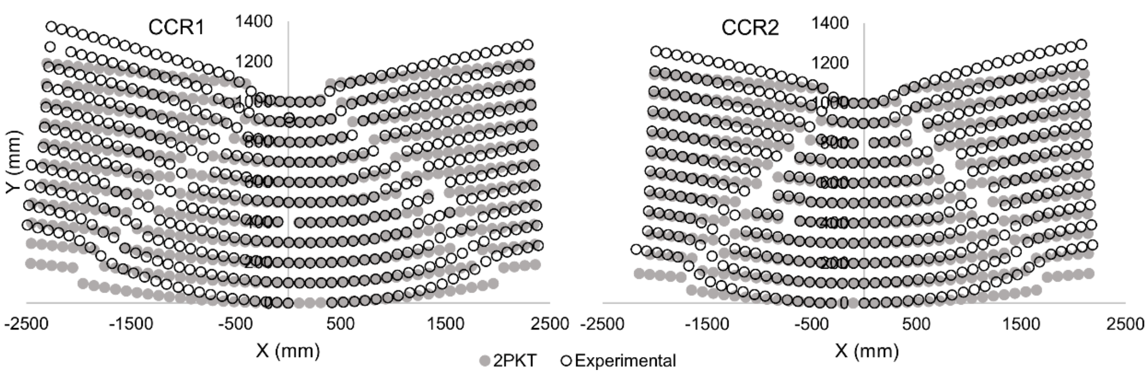

Figure 8. Comparison of deformation patterns obtained using DIC data with the predicted deformation using 2PKT at the peak load for CCR1 and CCR2 (×20 magnification).

The peak loads for the specimens were predicted using a modified version of the 2PKT that accounts for wide loading plates. See Proestos et al. (2021). The effective width of loading plate, l_{b1e} was calculated using Equation 1, where a_{cl} is clear shear span, h is total depth of the section, V is the shear force and P is the applied load. For asymmetrical loading cases, the peak shear was calculated for each span and the total load was determined from equilibrium.

$$l_{b1e} = 0.11\sqrt{a_{cl}^2 + h^2} \leq \min\,[370\,mm, \left(\frac{V}{P}\right) l_{b1} \quad (1)$$

The predicted peak loads for CCR1-CCR6 obtained using VecTor2 and the 2PKT were compared with the experimental peak loads (see Table 2 and Figure 3). The table shows that VecTor2 predicts the peak load for the six specimens with an average P_{exp}/P_{VT2} ratio of 1.10 and a 9.6% coefficient of variation.

The 2PKT predicts the peak load for the six specimens with an average P_{exp}/P_{2PKT} ratio of 1.03 with a 11.3% coefficient of variation. The results show that for the six specimens considered here, VecTor2 and the 2PKT can predict the peak load satisfactorily. Except for CCR5, the two methods are also capable of predicting the failure span correctly. This result likely arises from the fact that the south shear span of CCR5 has a shallower crack which results is smaller aggregate interlock than the north span where the crack is steeper. Additionally, the specific crack geometry on the north shear span has resulted a larger critical loading zone.

Table 2: Experimental peak load and predicted peak loads using VecTor2 and the 2PKT.

Specimen	P_{exp} (kN)	Failure span $_{exp}$	P_{VT2} (kN)	Failure span $_{VT2}$	P_{2PKT} (kN)	Failure span $_{2PKT}$	P_{exp}/P_{VT2}	P_{exp}/P_{2PKT}
CCR1	1916	South	1762	-	1847	-	1.09	1.04
CCR2	2235	North	1894	-	2069	-	1.18	1.08
CCR3	2614	South	2141	-	2355	-	1.22	1.11
CCR4	2333	North	2032	North	2025	North	1.15	1.15
CCR5	1765	South	1851	North	2073	North	0.95	0.85
CCR6	1816	North	1826	North	1969	North	0.99	0.92
						Average	1.10	1.03
						COV (%)	9.6	11.3

CONCLUSIONS

This paper presents data from a series, called the CCR series, of six large-scale, simply supported and monotonically loaded deep beam experiments which were monitored using full field of view Digital Image Correlation (DIC), throughout loading. The specimens consisted of symmetrical as well as asymmetrical loading conditions. The variables explored include the shear span-to-depth ratio, loading plate size and loading configuration. It was observed that as the shear span-to-depth ratio decreased, the ultimate strength of the specimens increased and the displacement at the ultimate load decreased. In asymmetrical loading cases, the strength of the specimen also depends on the influence of the offset load location on the effective shear span-to-depth ratio and effective loading plate size. This phenomenon manifests itself in the influence these variables have on critical crack angle, crack shape and crack location.

The paper presents the load-displacement response as determined from DIC measurements. The paper also presents the principal tensile and compressive strain fields obtained at the peak load for all six specimens. The tensile strain fields show the cracked regions, while the compressive strain fields show the highly compressed load transfer paths, commonly known as struts. The paper then presents the crack patterns on the west face of the specimen generated from the Automated Crack Detection and Measurement (ACDM) tool. These crack patterns show good agreement with the crack patterns observed on the east face of the specimens.

The experimental load-displacement data were compared with the predicted load-displacement response from VecTor2. While VecTor2 predicted uncracked stiffness satisfactorily, it predicted a somewhat stiffer cracked response than observed experimentally. The crack patterns were also compared with the predicted crack patterns using VecTor2. The VecTor2 models were able to satisfactorily predict the crack location and angles. The deformation pattern of the specimens obtained using DIC was used to evaluate the deformed shape predicted by the 2PKT and it was observed that the 2PKT predicted the deformations well. Comparison of the experimental peak load with VecTor2 predictions gave an average P_{exp}/P_{VT2} ratio of 1.10 and a coefficient of variation of 9.6%. Comparison of the experimental peak load with the 2PKT predictions gave an average P_{exp}/P_{2PKT} ratio of 1.03 with a coefficient of variation of 11.3%.

In conclusion, the results suggest that the data obtained from DIC can provide insightful information on the response of deep beams throughout loading. Additionally, VecTor2 and the 2PKT can provide good predictions of deep beams throughout loading. In the future, these experimental and numerical approaches can be used to guide the damage assessment of reinforced concrete nuclear facility components and in training digital twin technologies that maybe used to guide monitoring and repair of reinforced concrete structures.

REFERENCES

Campana, S., Fernández Ruiz, M., Anastasi, A. and Muttoni, A. (2013). "Analysis of shear-transfer actions on one-way RC members based on measured cracking pattern and failure kinematics," *Magazine of Concrete Research*, 65 (6), 386-404, 10.1680/macr.12.00142.

Collins, M. P. and Mitchell, D. (1991). *Prestressed Concrete Structures,* Englewood Cliffs, NJ: Prentice Hall.

Gheri, N., Mata-Falcón, J. and Kaufmann, W. (2020). "Automated crack detection and measurement based on digital image correlation," *Construction and Building Materials*, 256, 1-14. 10.1016/j.conbuildmat.2020.119383.

Langer M. (2019). *Evaluation of the Load-Bearing Mechanisms in Coupling Beams and Shear Walls based on DIC Measurements*, MSc thesis, University of Liège, Liège, Belgium, 136 pp.

Mata-Falcón, J., Haefliger, S., Lee, M., Galkovski, T. and Gheri, N. (2020). "Combined application of distributed fibre optical and digital image correlation measurements to structural concrete experiments," *Engineering Structures*, 225. 10.1016/j.engstruct.2020.111309.

Mihaylov, B. I., Bentz, E. C. and Collins, M. P. (2013). "Two-Parameter Kinematic Theory for Shear Behavior of Deep Beams," *ACI Structural Journal*, 110 (3), 501-509.

Palipana, D. K., Trandafir, A. N., Mihaylov, B. I. and Proestos, G. T. (2021). "Quantification of Shear Transfer Mechanisms of Reinforced Concrete Deep Beams," *fib Symposium 2021*, Lisbon, Portugal, 14-16.

Palipana, D. K., Trandafir, A. N., Mihaylov, B. I. and Proestos, G. T. (2022). "Framework for Quantification of Shear Transfer Mechanisms from Deep Beam Experiments," *ACI Structural Journal*, 119 (3). 10.14359/51734485.

Popovics, S. (1970). "A review of stress-strain relationships for concrete," *ACI Structural Journal*, 67 (3), 243-248.

Proestos, G. T., Bentz, E. C. and Collins, M. P. (2018). "Maximum Shear Capacity of Reinforced Concrete Members," *ACI Structural Journal*, 115 (5), 1463-1473. 10.14359/51702252.

Proestos, G. T., Palipana, D. K. and Mihaylov, B. I. (2021). "Evaluating the shear resistance of deep beams loaded or supported by wide elements," *Engineering Structures*, 226, 111368. 10.1016/j.engstruct.2020.111368.

Qambar, M. (2020). *Effect of Wide Loading Elements and Shear Span-to-Depth Ratio on the Behavior of Shear Critical reinforced Concrete Deep Beams*, MSc thesis, North Carolina State University, Raleigh, NC, 268 pp.

Spencer, B. F., Hoskere, V. and Narazaki, Y. (2019). "Advances in computer vision-based civil infrastructure inspections and monitoring," *Engineering*, 5 (2), 199-222.

Sutton, M. A., Orteu, J., and Schreier, H. W. (2009). *Image Correlation for Shape, Motion and Deformation Measurements. Basic Concepts, Theory and Applications,* Springer. 10.1007/978-0-387-78747-3.

Trandafir, A. N., Palipana, D. K., Proestos, G. T. and Mihaylov, B. I. (2022). "Framework for Crack-based Assessment of Existing Lightly reinforced Concrete Deep Members," *ACI Structural Journal*, 119 (1), 10.14359/5173143.